Surface Heat Budgets and Sea Surface Temperature in the Pacific Warm Pool during TOGA COARE

Shu-Hsien Chou
NASA Goddard Space Flight Center
Greenbelt, Maryland

Wenzhong Zhao
Space Applications Corporation
Largo, Maryland

Ming-Dah Chou
NASA Goddard Space Flight Center
Greenbelt, Maryland

To be submitted to Journal of Climate
September 1998

Corresponding author: Dr. Shu-Hsien Chou, Code 912, Laboratory for Atmospheres, NASA Goddard Space Flight Center, Greenbelt, MD 20771.
E-mail: chou@agnes.gsfc.nasa.gov

ABSTRACT

The daily mean heat and momentum fluxes at the surface derived from the SSM/I and Japan's GMS radiance measurements are used to study the temporal and spatial variability of the surface energy budgets and their relationship to the sea surface temperature during the COARE intensive observing period (IOP). For the three time legs observed during the IOP, the retrieved surface fluxes compare reasonably well with those from the IMET buoy, RV Moana Wave, and RV Wecoma. The characteristics of surface heat and momentum fluxes are very different between the southern and northern warm pool. In the southern warm pool, the net surface heat flux is dominated by solar radiation which is, in turn, modulated by the two Madden-Julian oscillations. The surface winds are generally weak, leading to a shallow ocean mixed layer. The solar radiation penetrating through the bottom of the mixed layer is significant, and the change in the sea surface temperature during the IOP does not follow the net surface heat flux. In the northern warm pool, the northeasterly trade wind is strong and undergoes strong seasonal variation. The variation of the net surface heat flux is dominated by evaporation. The two westerly wind bursts associated with the Madden-Julian oscillations seem to have little effect on the net surface heat flux. The ocean mixed layer is deep, and the solar radiation penetrating through the bottom of the mixed layer is small. As opposed to the southern warm pool, the trend of the sea surface temperature in the northern warm pool during the IOP is in agreement with the variation of the net heat flux at the surface.

1. Introduction

The western tropical Pacific is characterized by the highest sea surface temperature (SST) and heavy rainfall in the world ocean. A small variation of SST associated with the eastward shift of the warm pool during El-Nino/Southern Oscillation events changes the atmospheric circulation pattern and affects the global climate. The change in the SST pattern in the warm pool for a time scale longer than a year is related to the ocean dynamics in the Pacific basin. For a seasonal time scale and shorter, on the other hand, the SST in the warm pool is determined by the surface fluxes and the depth of the ocean mixed layer, which are affected by the variations in the surface wind and clouds.

In a study of the depth of ocean mixed layer with a uniform density in the Pacific warm pool, Lukas and Lindstrom (1991) have found that the mixed layer in this region is very shallow with a mean of ~29 m. The shallow mixed layer reduces the solar heating of the layer because of the enhanced penetration of solar radiation through the bottom of the layer. Between the bottom of the mixed layer and the top of the thermocline, there is a barrier layer characterized by nearly constant temperature with stable stratification due to downward increase of salinity. This stable barrier layer inhibits the entrainment of cold water from the deeper thermocline except during very strong westerly wind bursts. The horizontal advection of heat in the warm pool has been estimated to be very small due to a small SST gradient and weak currents (Niiler and Stevenson, 1982; Enfield, 1986; Godfrey and Linstrom, 1989). Thus, the change in the warm pool SST in seasonal time scale and shorter is primarily determined by the net surface heat flux, penetration of solar radiation through the bottom of the mixed layer, and the mixed-layer depth (Anderson et al. 1996; Sui et al. 1997).

In recognition of the importance of the Pacific warm pool in affecting the global climate, extensive measurements were carried out during the Intensive Observing Period (IOP), from November 1992 to February 1993, of the Tropical Ocean Global Atmosphere

(TOGA) Coupled Ocean-Atmosphere Response Experiment (COARE) with the major objective of better understanding various physical processes responsible for the SST variation (Webster and Lukas, 1992). Various flux measurement programs were carried out at the Intensive Flux Array (IFA) within the region 1°N-5°S and 150°E-160°E during the IOP. Radiative, turbulent, and freshwater fluxes at the surface were either directly measured or derived from the measurements of surface temperature, humidity, and winds at the IMET buoy (1.75°S, 156°E) and two research vessels (RV) Moana Wave (1.7°S, 156°E) and Wecoma (cruised in a butterfly pattern around the IMET). These high temporal resolution fluxes are very useful for studying the air-sea interaction and for validating the satellite retrievals of surface radiative and turbulent fluxes.

In the western equatorial Pacific, the surface winds are weak and are interrupted intermittently by westerly wind bursts. These westerly wind bursts are often related to the Madden-Julian oscillations (MJOs) which have a period of ~40-50 days. During the COARE IOP, there were two MJOs propagating eastward from the Indian Ocean to the Central Pacific (Gutzler et al. 1994; Lin and Johnson 1996; Lau and Sui 1997; Sui et al. 1997). Two envelopes of individual cloud clusters and two low-level westerly wind bursts lasting for about 2-3 weeks were associated with the two MJOs. The super cloud clusters reduce solar heating, while the westerly wind bursts enhance the evaporative cooling. Both have an important impact on the SST variation of the warm pool.

In a study of the radiation budgets of the Pacific warm pool, Chou et al. (1998) applied empirical relationships between the surface-measured radiative fluxes and the satellite-measured radiances to compute the solar and thermal infrared fluxes over the Pacific warm pool for the COARE IOP. Chou et al. (1997) computed daily mean turbulent fluxes at the surface with a stability-dependent bulk scheme. The surface wind and humidity retrieved from the radiances measured by the Special Sensor Microwave/Imager (SSM/I) were used. We use these fluxes to study the relationship between the SST and the air-sea fluxes. The methods for deriving the surface fluxes and

the sources of data used in this study are briefly described in Section 2. In Section 3, the accuracy of the satellite-retrieved surface fluxes is assessed using independent measurements at the IMET buoy, RV Moana Wave, and RV Wecoma during the IOP. Section 4 investigates the spatial distributions of the surface heat budgets, as well as the relevant parameters used for deriving the surface fluxes. The impacts of the two MJOs on the surface heat budget and the contrast between the northern and southern warm pool are discussed. Section 5 examines the relation of the SST variation to the heat and momentum fluxes at the surface and the penetration of solar flux through the bottom of the ocean mixed layer. Conclusions are given in Section 6.

2. Data sources

The daily mean surface momentum, latent heat, and sensible heat fluxes computed by Chou et al. (1997) have a spatial resolution of 2°x2.5° latitude-longitude over global oceans and cover the period July 1987-December 1994. To be consistent with the spatial resolution of the radiative fluxes used in this study (to be discussed below), we linearly interpolate these fluxes onto a 1°x1° latitude-longitude grid in the Pacific warm pool (defined as 10°S-10°N, 135°E-175°E hereafter) for the IOP.

These turbulent fluxes were derived from daily mean values of SST, specific humidity and wind speed 10 m above the sea surface, and air temperature 2 m above the sea surface, using a stability-dependent aerodynamic bulk scheme. The 10-m wind speeds and water vapor amount in the entire atmospheric column were derived by Wentz (1994) from radiances measured by the SSM/I on board the Defense Meteorological Satellite Program (DMSP) F10 and F11 polar-orbiting satellites, which had ascending equatorial crossings at 1942 and 1742 LT, respectively. The 10-m specific humidity was derived from the water vapor amount in the entire atmospheric column of Wentz (1994) and the lowest 500-m layer above the surface using the method developed by Chou et al. (1995, 1997). The latter was retrieved from the SSM/I radiances using the method of Schulz et al. (1993). Wind stress directions were taken from the surface wind directions

of Atlas et al. (1996) which used the SSM/I surface wind speed of Wentz (1994) for the analysis. These SSM/I-retrieved surface winds and water vapor amounts had an original spatial resolution of $(25\ km)^2$. They were degraded to daily means and 2°x2.5° latitude-longitude regions separately for the DMSP F10 and F11 satellites. Two sets of fluxes were first computed for these two satellites separately and then averaged to form the daily mean fluxes. The SST data used for computing latent heat fluxes were taken from the National Center for Environmental Prediction (NCEP). Daily SSTs were interpolated from the weekly mean values with a spatial resolution of 1°x1° latitude-longitude (Reynolds and Smith, 1994). The difference in the SST and the temperature at the 2-m height, SST - T_{2m}, used for computing the sensible heat flux was taken from the European Centre for Medium-Range Weather Forecasts (ECMWF) analysis, which had a spatial resolution of 2°x2.5° latitude-longitude and a temporal resolution of 12 hr.

The surface radiative fluxes computed by Chou et al. (1998) are used in this study. Chou et al. (1998) derived empirical relationships between the radiances measured by the Japan's Geostationary Meteorological Satellite (GMS) and the surface radiative fluxes measured at several radiation sites during the IOP. The downward shortwave flux at the surface was computed as a function of the satellite-measured albedo in the visible channel and the solar zenith angle. When data of visible albedo were missing, the satellite-measured brightness temperature in the IR window channel was used. The downward longwave flux was computed as a function of SST, the total column water amount and the brightness temperature in the GMS IR window channel. These empirical relationships were applied to derive the surface solar and thermal infrared fluxes in the western Pacific warm pool. The retrieved radiative fluxes originally had a spatial resolution of $(35\ km)^2$ and a temporal resolution of 1 hr. They were subsequently degraded to daily values with a 1°x1° latitude-longitude spatial resolution.

To validate the satellite-retrieved surface fluxes, we use the turbulent fluxes derived from the meteorological measurements and the radiative fluxes measured at the IMET, RV

Moana Wave, and RV Wecoma (Weller and Anderson, 1996). Fairall et al. (1996) derived the turbulent fluxes directly from the high frequency temperature, humidity, and wind measurements at the RV Moana Wave and developed an aerodynamic bulk scheme for estimating turbulent fluxes in weak wind and convective situations. This bulk scheme was applied to derive the fluxes at IMET and RV Wecoma. Weller and Anderson (1996) found that the surface fluxes at the IMET buoy were in good agreement with those at the nearby Wecoma and Moana Wave. It is noted that the data used to derive the empirical relationships between the satellite radiance measurements and the surface radiative flux measurements do not include the data from IMET, Moana Wave, and Wecoma. Thus, radiative fluxes measured at these three surface platforms and those derived from the satellite-measured radiances are independent and suitable for intercomparison.

3. Collocation validation

The surface heat and momentum fluxes derived from satellite measurements are compared with that derived from observations at the IMET buoy (1.75°S, 156°E). Mean fluxes of two 1°x1° latitude-longitude regions centered at (1.5°S, 155.5°E) and (1.5°S, 156.5°E) are used for the comparison with the IMET observations. The net heat flux at the surface F_{net} is defined as $F_{net} = F_{SW} - (F_{LW} + F_{SH} + F_{LH})$, where F_{SW} is the net downward solar (shortwave) flux, F_{LW} is the net upward infrared (longwave) flux, F_{SH} is the upward sensible heat flux, and F_{LH} is the latent heat flux (evaporative cooling). Figure 1 and Table 1 compare daily mean surface fluxes from the IMET buoy (solid lines) and retrievals (dashed lines, pluses and diamonds) during the IOP. Note that the surface fluxes at the IMET buoy are slightly different from those presented in Weller and Anderson (1996). In Table 1, the daily SD error denotes the standard deviation of daily differences of fluxes between the retrieval and IMET, while the monthly and IOP SD errors are derived with the assumption that daily SD errors are random. The biases and the monthly and IOP SD errors of the retrieved surface fluxes provide us the information on the uncertainty of the monthly and IOP mean surface heat budgets.

The net solar fluxes at the surface shown by pluses (70 days) in Fig. 1a are retrieved from the visible albedo, while those shown by diamonds (50 days) are retrieved from the IR brightness temperature when there are no albedo data available. It can be seen that the solar fluxes retrieved from the brightness temperature and the albedo have comparable accuracy. The satellite-retrieved solar flux is generally in good agreement with that measured at the IMET, except large discrepancies on some days with strong and weak solar radiation. The retrieved solar fluxes are averaged over two 1°x1° latitude-longitude regions containing the IMET site, whereas the area of the sky which contributes to the solar flux measured at the surface is much smaller, <10 km. Because of the difference in spatial resolution, the satellite-retrieved solar flux is less sensitive to the distribution of clouds in the vicinity of the surface site than the surface measurements. It follows that the former is smoother in time than the latter, which can partially explain the relatively large discrepancies at both large and small solar fluxes. The daily mean solar flux fluctuates between 50 and 270 W m^{-2}. Table 1 shows that the retrieved F_{SW} has a mean of 196.6 W m^{-2}, with a bias of 1.8 W m^{-2}, an SD error of 32.5 W m^{-2} for the daily mean flux, and a correlation coefficient of 0.86 between the satellite retrievals and surface observations.

Figure 1b shows that the net longwave flux is much smaller than the solar flux and fluctuates within a small range between 40 and 75 W m^{-2}. Table 1 shows that the retrieved F_{LW} has a mean of 50.9 W m^{-2}, with a bias of -7.1 W m^{-2}, an SD error of 5.2 W m^{-2} for the daily mean flux, and a correlation coefficient of 0.75 between the satellite retrievals and surface observations. To investigate the relatively large bias of net longwave flux, we examine separately the upward ($F\uparrow$) and downward ($F\downarrow$) components of the net longwave flux, which is given by

$$F_{LW} = F\uparrow - F\downarrow = [(\varepsilon \sigma T^4_S + (1 - \varepsilon) F\downarrow] - F\downarrow, \quad (1)$$

where ε is the emissivity of sea surface, σ is Stefan-Boltsman constant, and T_S is the SST. The emissivity is taken to be 0.97 in computing the net longwave flux at the IMET

(Weller ad Anderson 1996), whereas it is taken to be 1 in this study for the satellite-retrieved net longwave flux. The difference in ε only induces a difference of 2 W m^{-2} in F_{LW}. Averaged over the IOP, the NCEP SST (302.5 K) of the two comparison grid points used to compute the retrieved F_{LW} is 0.4 K higher than the skin temperature of sea surface used to compute F_{LW} at IMET, which will cause at most a difference of about 2 W m^{-2} in F_{LW}. The mean values of $F\uparrow$ (475.4 W m^{-2}) and $F\downarrow$(424.4 W m^{-2}) of the satellite retrievals are larger than those at IMET by 4 and 11 W m^{-2}, respectively. Thus, the negative bias of F_{LW} is mainly due to a 2.6% overestimation of the satellite-retrieved $F\downarrow$.

The satellite-retrieved and surface-measured sensible heat fluxes are shown in Fig. 1c. The retrieval significantly underestimates the peak values of sensible heat flux during westerly wind bursts and squalls. It is the result of a smaller sea-air temperature difference of the ECMWF analysis and a smaller satellite-retrieved wind speed than those measured at IMET. Although the percentage error is large, the magnitude of the bias is small. Table 1 shows that the retrieved F_{SH} has a mean of only 6.3 W m^{-2}, a bias of -2.6 W m^{-2}, and an SD error of 1.1 W m^{-2} (0.6 W m^{-2}) for the monthly (IOP) mean sensible heat flux.

Figures 1d and 1e show that the retrieved latent heat flux and wind stress are generally in good agreement with those measured at IMET. However, for those days with a large negative bias of sensible heat flux during westerly wind bursts and squalls, the retrieval also underestimates peak values of evaporative cooling and wind stress. The underestimation of speed during high winds might be a result of spatial and temporal variability. The daily mean turbulent fluxes at IMET were computed from the measured hourly local wind. However, the retrieved daily mean fluxes are the averages of retrieved fluxes using measurements from the DMSP F10 and F11 satellites, which had ascending equatorial crossings at 1942 and 1742 LT, respectively. Furthermore, the retrieved daily fluxes of the two finer resolution grid points used for the comparison are interpolated

from those of four neighboring grid points each with a coarser resolution of 2°x2.5° latitude-longitude. The latter fluxes for each satellite are computed from the available wind speeds averaged over a day and a domain of 2°x2.5° latitude-longitude, which tends to smooth the peak value of the wind speed. It may also be a result of the error in wind retrieval induced by rainfall contamination, as precipitation is commonly associated with westerly wind bursts and squalls. Table 1 shows that the latent heat flux has a mean of 104.8 W m^{-2}, with a bias of -2.4 W m^{-2}, an SD error of 29.1 W m^{-2} for the daily mean flux, and a correlation coefficient of 0.71; while the wind stress has a mean of 0.0371 N m^{-2}, with a bias of -0.0018 N m^{-2}, an SD error of 0.0210 N m^{-2} for the daily mean wind stress, and a correlation coefficient of 0.78.

The net heat flux at the surface is shown in Figure 1f. Except for the large discrepancies on certain days with either large or small values of the net heat flux measured at IMET, the two sets of the net heat flux are generally in good agreement. The daily mean net heat flux fluctuates between -200 and 150 W m^{-2} for the measurements, but fluctuates between -150 and 200 W m^{-2} for the retrieval. Table 1 shows that the retrieved net heat flux has a mean of 34.6 W m^{-2}, a bias of 13.8 W m^{-2}, an SD error of 48.2 W m^{-2} for the daily mean flux, and a correlation coefficient of 0.82.

To further validate the retrieved surface fluxes, we show in Table 2 the satellite-retrieved (Sat) surface fluxes with those from the RV Moana Wave (MW), RV Wecoma (Wec), and the IMET buoy for the periods during three legs of the RV Moana Wave observation, which are shaded in Fig. 1. Weller and Anderson (1996) pointed out that Leg 1 (14 November 1992 - 3 December 1992) was characterized by clear skies and large spatial scales of low winds within the IFA. Leg 2 (20 December 1992 - 11 January 1993) started with strong westerly wind bursts across the IFA and then shifted back to clear skies with fairly uniform light winds in January 1993. Leg 3 (27 January 1993 - 3 February 1993) was characterized by eastward propagating surges of westerlies and scattered clouds. There is significant variability among the three legs. The net surface

heating for the ocean is positive during Leg 1, as a result of smaller cloudiness and low wind. On the other hand, the net heating is negative for the other two legs, due to reduced solar heating and strong evaporative cooling associated with westerly wind bursts (Leg 2) and squalls (Leg 3). The retrieved fluxes agree reasonably well with those measured at the three surface platforms.

4. Spatial Distributions of Surface Heat Budgets

Components of the surface heat budget averaged over the COARE IOP are shown in Fig. 2, and the relevant parameters for computing surface fluxes are shown in Fig. 3. These fluxes and parameters averaged over individual months and the IOP are shown in Table 3. Figures 2a and 3a show the surface net solar flux (F_{SW}) and IR brightness temperature (T_B) for the warm pool averaged over the IOP, respectively. The spatial distributions of F_{SW} and T_B are very similar, as both are dominated by clouds; strong convective activities are associated with low solar flux and IR brightness temperature. The shaded areas in the eastern warm pool and New Guinea, where F_{SW} <190 W m^{-2} and T_B<267.5 K, indicate regions of strong deep convection. There are two regions of maximum cloudiness east of 160°E and centered at 4°N and 4°S. The northern branch of the maximum cloudiness is stronger than the southern branch and extends westward across the warm pool. The minimum F_{SW} and T_B located near the dateline indicates that the deep convection center or the upward branch of the Walker circulation shifted eastward by about 60° longitude during the COARE IOP from its normal location at ~120°E-130°E. The solar flux varies between 170 and 210 W m^{-2} and is ~ 200 W m^{-2} over the IFA. The maximum F_{SW} to the north and east of New Guinea indicates that these regions are persistently dry. It probably is caused by the descending mesoscale circulation induced by the strong convection over New Guinea where topography is high and solar heating of the land surface is large. Averaged over the warm pool and the IOP, the solar heating of the ocean is 192.9 W m^{-2}.

Figure 2b shows that both the magnitude and variation of the net IR cooling of the warm pool are small. The pattern of the net upward IR flux (F_{LW}) is negatively correlated with that of total precipitable water (not shown), and the increases of F_{LW} by about 10 W m^{-2} from 53 W m^{-2} at 5°N to 63 W m^{-2} at 10°N is due to a reduced column water vapor amount, W, from 5.2 cm at 5°N to 4 cm at 10°N. Clouds do not have a significant effect on the surface IR flux, as high humidity (see Table 3) makes the atmosphere very opaque to the longwave radiation..

Figures 2c, 3b and 3c show the latent heat flux, 10-m surface wind speed (U_{10m}) and sea-air humidity difference (Q_S-Q_{10m}) averaged over the COARE IOP, respectively. The latent heat flux is the second largest heat budget component and is equal to 131.9 W m^{-2} when averaged over the warm pool and the IOP (Table 3). It is large mainly due to a large sea-air humidity difference. The spatial variability of latent heat flux is the largest among the budget components, varying between 90 and 220 W m^{-2}, as a larger sea-air humidity difference is coupled with a larger wind speed and vise versa. The (Q_S-Q_{10m}) is about 4.5-5.2 g kg^{-1} south of ~ 3°N and west of 160°E but increases northward to about 6.4 g kg^{-1} at 10°N, with a mean of 5.4 g kg^{-1} for the warm pool. The wind speed is about 5 m s^{-1} south of 3°N and increases northward to about 9 m s^{-1} at 10°N, with a mean of 6.1 m s^{-1} for the warm pool. This increase in wind speed reflects a northward strengthening of the NE trade winds. Note that the mean wind speed is scalar averaged, not a vector mean of wind velocity. Thus it should be larger than the magnitude of vector mean of wind velocities over the IOP, especially over the area south of 3-4°N where winds are weak and highly variable. The latent heat flux in the IFA is about 105 W m^{-2} and is relatively small as compared to the values of 150-220 W m^{-2} over the trade wind region in the northern warm pool.

Figures 2d and 3d show the sensible heat flux and sea-air temperature difference (SST-T_{2m}) averaged over the IOP, respectively. The sensible heat flux is the smallest heat budget component and is equal to 6.9 W m^{-2} when averaged over the warm pool and the

IOP (Table 3). It is very small as the sea-air temperature difference is very small. The spatial variability of sensible heat flux is also very small, due to the offsetting effect between sea-air temperature differences and wind speeds (Figs. 3b and 3d). The (SST-T_{2m}) is about 1-1.4 °C in the 5°S-5°N band and decreases poleward to about 0.4 °C at 10°N, with a mean of 0.9 °C for the warm pool.

Two 40-50 days MJOs associated with super cloud clusters and westerly wind bursts were observed to propagate eastward from the Indian Ocean to the Central Pacific during the IOP. The super cloud clusters reduce solar heating, while the westerly wind bursts enhance evaporative cooling. The first MJO was associated with stronger convection, evaporative cooling and SST cooling with the maximum impacts over the southern warm pool, as compared to the second MJO (see section 5). The Walker circulation associated with the first and second MJOs generally had sinking motion over the southern warm pool and rising motion over Indian Ocean during November 1992 and January 1993, respectively. This situation was reversed during December 1992 and February 1993 when regions of rising motion moved into the warm pool. The impacts of these two MJOs on the temporal and spatial variability of the surface heat budget and SST are investigated below.

It can be seen in Fig. 4 that the super cloud clusters associated with these two MJOs have a significant impact on the monthly variability of solar heating. The impact is especially large in the southern warm pool. Figures 4a and 4c show that convection was generally suppressed with larger solar heating in the southern warm pool during November 1992 and January 1993 as affected by the sinking motions of the two MJOs, while the convection in the northern intertropical convergence zone in the northern warm pool appeared to be intensified. When the super cloud clusters moved into the warm pool in December 1992 and February 1993, the surface solar heating decreased greatly in the southern warm pool, especially for the cloud band 0-7°S in December 1992. The mean solar heating of the southern warm pool decreases by 40 W m^{-2} from November 1992 to

December 1992 and by 30 W m^{-2} from January 1993 to February 1993. These results show that the super cloud clusters associated with the eastward propagating MJOs cause significant local variability of the solar heating, reaching 50 W m^{-2}, on monthly scale.

The monthly and spatial variability of latent heat flux as shown in Fig. 5 is quite different from that of solar heating. In the southern warm pool, the impact of the two MJOs on the latent heat flux is smaller than the impact on the solar heating. The first westerly wind burst is very strong. Averaged over the southern warm pool, it enhances the 5-day mean latent heat flux by ~100 W m^{-2} during its peak period (see Fig. 9). However, the abrupt increase in the latent heat flux lasts only for 12 days in late December 1992 and early January 1993. The second westerly wind burst is rather weak and is associated with a reduced sea-air humidity difference. The impact on the monthly mean latent heat flux is small, ~20 W m^{-2}.

In the northern warm pool, on the other hand, the monthly latent heat flux increases significantly in December 1992 and January 1993, as a result of the intensification of the NE trade winds (not shown in the figures). In these two months, the latent heat flux is very large with the most tight gradient varying from 130 to 270 W m^{-2} across the 3°N-10°N band. It increases by ~50-120 W m^{-2} from November 1992 to January 1993 due to the strengthening of the NE trade wind coupling with increased sea-air humidity difference, which are associated with the southward shift of the trade wind belt. Averaged over the southern and northern warm pool, the monthly mean latent heat fluxes are 114.7, 151.4, 138.4, and 121.4 W m^{-2} for the four IOP months, respectively (Table 3). The large monthly variability of the warm-pool mean latent heat flux is modulated by the trade winds over the northern domain of the warm pool.

Monthly variability of the net surface heat flux is shown in Fig. 6. The variability is mainly determined by that of solar heating in the southern warm pool and by the evaporative cooling in the northern warm pool. The IOP is a winter season in the northern hemisphere but is a summer season in the southern hemisphere. Thus, wide-

spread net heating occurs in the southern warm pool during the entire IOP except for the cooling in the regions east of 160°E and north and south of New Guinea in December 1992 affected by the first MJO. Net cooling is confined nearly entirely to the northern warm pool. The strong cooling reaching a magnitude >100 W m^{-2} occurs near the northern edge of the warm pool in December 1992 and January 1993, mainly due to enhanced evaporative cooling as a result of the strengthening of the NE trade wind associated with the southward shift of the trade wind belt as discussed above. Averaged over the warm pool, monthly mean net heat fluxes are 20.9, -26.7, -2.9, and 13.7 W m^{-2} for November 1992, December 1992, January 1993, and February 1993, respectively (Table 3). The mean heating of the warm pool during the IOP is only 0.7 W m^{-2}.

5. Relation of SST Variation to Surface Fluxes

The rate of change in the temperature of the ocean mixed layer or the SST is determined by the heat convergence and the depth of the mixed layer. The former involves the net heat flux at the surface, advection of heat by ocean currents, as well as the transmission of solar radiation and the entrainment of cold water through the bottom of the mixed-layer. The western equatorial Pacific is characterized by frequent heavy rainfall and weak mean winds with highly intermittent westerly wind bursts. The mixed layer with constant density has been observed to be generally very shallow. Beneath it is a nearly isothermal barrier layer where density increases with depth due to salinity that inhibits the entrainment of cold water from the thermocline into the mixed layer except during strong westerly wind bursts (Lukas and Linstrom 1991; Anderson et al. 1996). The horizontal advection of heat in the warm pool has been found to be very small due to weak SST gradients and currents (Niiler and Stevenson 1982; Enfield 1986; Godfrey and Lindstrom 1989).

Assuming that the advection of heat and entrainment of cold water are negligible, the heat budget of the mixed-layer may be written as

$$h \rho C_P (\partial T_S/\partial t) = F_{net} - f(h) F_{SW}, \quad (2)$$

where h is the mixed-layer depth, ρ is the density of sea water (10^3 kg m^{-3}), C_P is the heat capacity of sea water at constant pressure (3.94 x 10^3 J kg^{-1} $°C^{-1}$), $\partial T_S/\partial t$ is the rate of change in the SST, and f (h) is the fraction of F_{SW} penetrating through the depth h. Using the water "type 1A" data of Jerlov (1968), Paulson and Simpson (1977) derived f (h) as

$$f(h) = \gamma e^{-\alpha h} + (1-\gamma) e^{-\beta h}, \quad (3)$$

where γ is 0.62, α is 1.6 7 m^{-1}, and β is 0.05 m^{-1}. In (3), the solar spectrum at the sea surface is divided into two groups, one corresponding to the ultraviolet and visible region and the other corresponding to the near infrared region. The weights of the energy contained in these two spectral regions are γ and 1- γ, and the absorption coefficients of sea water are α and β, respectively. Using daily values of $\partial T_S/\partial t$, F_{net}, and F_{SW}, we solve (2) and (3) for h and f (h) F_{SW}. It is noted that during the period of 11-21 January 1993, most of the solutions of h and f(h) F_{SW} north of 5°N cannot be obtained and are spatially interpolated. The missing solution may be due to errors in the retrieved daily surface fluxes and SST, which is interpolated from the weekly SSTs. It may also be a result of neglecting heat transports by ocean currents in estimating the mixed-layer heat budgets.

The spatial distributions of F_{net} and $\partial T_S/\partial t$ averaged over the IOP are shown in Figs. 7a and 7b, respectively. As expected, the ocean gains heat in the summer (southern) hemisphere while loses heat in the winter (northern) hemisphere, with the net heat flux ranging from -80 W m^{-2} in the northeastern section of the warm pool to 40 W m^{-2} north of New Guinea. Averaged over the warm pool, the net heating is only 0.7 W m^{-2}. This result is consistent with the studies of Godfrey and Lindstrom (1989) and Godfrey et al. (1991) that the mean surface net heat flux into the warm pool is small (<10 W m^{-2}). On the other hand, Fig. 7b shows that, except near the southern edge, the warm pool cools during the

IOP. The cooling increases northward and reaches a maximum >0.5 °C $month^{-1}$. Averaged over the warm pool, the SST cools at a rate of 0.14 °C $month^{-1}$, which does not agree with a 0.7 W m^{-2} of net heat flux at the surface. This discrepancy is particularly large in the southern warm pool. For example, the net surface heat flux north of New Guinea has a maximum >40 W m^{-2}, but the SST cools at a rate of 0.3 °C $month^{-1}$. This is an indication that much of the solar flux incident at the surface penetrates through the bottom of the mixed layer and is not available for heating the layer.

Figure 7c shows the estimated solar flux penetrating through bottom of the mixed layer, $f(h)F_{sw}$, averaged over the IOP. Averaged over the IOP, the solar radiation lost through the bottom of the mixed layer is ~26 W m^{-2} for the northern warm pool and ~45 W m^{-2} for the southern warm pool. The domain-averaged value of 35 W m^{-2} is significantly larger than the net surface heat flux of 0.7 W m^{-2}. Thus, the cooling of SST in the warm pool during the IOP is primarily due to this loss of solar radiation, although the infrequent westerly wind bursts may deepen the mixed layer to the top of the thermocline and entrain cold water from below.

The mixed-layer depth h and the scalar-averaged wind stress τ averaged over the IOP are shown in Figs 8a and 8b, respectively. The mean wind stress directions are also shown in Fig. 8b. The pattern of h follows closely that of τ. In the northern warm pool, h and τ increase northward. In the southern warm pool, h and τ are rather uniform. In the vicinity of the IMET buoy, the estimated h is 28 m, which agrees reasonably well with the mean mixed-layer depth of 15 m measured during the IOP (Anderson et al. 1996). Averaged over the southern warm pool, the estimated h is 35 m, which also compares well with the mean mixed-layer depth of 29 m measured by Lukas and Lindstrom (1991) in the equatorial western Pacific.

The similarity between h and τ indicates that the mixed layer in the warm pool is mainly driven by winds. Winds supply turbulent kinetic energy for mixing and thus

deepen the mixed layer. On the other hand, both positive downward heat and fresh water (precipitation minus evaporation) fluxes at the surface reduce the density of water and supply a positive surface buoyancy flux, which inhibits mixing and thus reduces the depth of mixed layer. For the case of positive surface buoyancy forcing with insignificant entrainment cooling, the mixed-layer depth is proportional to u_*^3 and inversely proportional to the surface buoyancy flux (Niiler and Kraus 1977; Anderson et al. 1996), where u_* is the friction velocity proportional to the square root of the wind stress. Anderson et al. (1996) found that the surface buoyancy forcing on the mixed-layer of the warm pool was generally positive and varied little on timescales longer than 2 days. It is a result of the fact that negative buoyancy forcing, due to surface cooling caused by westerly wind bursts and squall events, is accompanied by positive buoyancy forcing, due to positive fresh water flux from heavy rain. The near-constant positive surface buoyancy forcing suggests that the mixed-layer depth is dependent primarily on the wind forcing.

We have analyzed the two MJOs using the time-longitude sections of daily IR brightness temperature and surface zonal wind averaged over the 0-10°S band from 80°E to 160°W for the COARE IOP (not shown). There were two super cloud clusters with T_B<253K and two westerly wind bursts with 10-m westerly zonal wind of 5-12 m s^{-1} covering a zonal width of 20°-40° longitude associated with two MJOs propagating eastward with a speed of 3.6 m s^{-1} from the Indian Ocean to the Central Pacific. The two westerly wind bursts moved through the southern warm pool during the periods from 20 December 1992 to 5 January 1993 and from 28 January 1993 to 28 February 1993 with the super cloud clusters right ahead of them. To further study the impacts of these two MJOs on the surface heat budgets and SST evolutions, we have analyzed the time series of 5-day running means of SST, surface and mixed-layer heat budgets, scalar-averaged wind stress, and mixed-layer depth averaged over the southern and northern warm pool, separately. The results are shown in Fig. 9 for the former and Fig. 10 for the latter.

Figure 9a shows that the SST in the southern warm pool is modulated by the two MJOs, with the maximum SST near 9 December 1992 and 20 January 1993. During the period from 5 November 1992 to 9 December 1992, the ascending branch of the first MJO was over the Indian ocean while the southern warm pool was in the dry descending phase. Figure 9b and 9c show that the sky was generally clear with little cloud and that easterly winds are weak as indicated by the large F_{SW} and the small F_{LH} and τ. Convection intensified from 10 December 1992 to 24 December 1992 as the super cloud cluster and wet phase of the first MJO moved into the southern warm pool from the Indian Ocean as indicated by the decreasing F_{SW}, while F_{LH} and τ associated with weak convergent winds remained small. Convection weakened from 25 December 1992 to 5 January 1993 as the super cloud cluster departed from the warm pool to the central Pacific and induced the strongest westerly wind burst, as indicated by the maximum F_{LH} and τ, with sinking motion over the southern warm pool. The maximum westerly wind (or F_{LH}) was induced by the strong convection centered around the dateline where the SST is very high. Thus, in the southern warm pool, the maximum westerly wind (or maximum F_{LH}) lagged the most intense convection (or minimum F_{SW}) by ~ 9 days. The maximum westerly wind lagged the warmest SST by 25 days and led the coldest SST by 5 days. These phase relationships are in good agreement with previous findings based on the observations from the IMET buoy (Lin and Johnson 1996; Lau and Sui 1997), as the first MJO is spatially very coherent.

The second MJO started with dry descending phase on 6 January 1993 but lasted for only a short period until about 27 January 1993. It is noted that the minimum F_{SW} and the maximum F_{LH} on 20 January 1993 are not related to the westerly wind burst but are caused by the relatively strong southeasterly trade wind. Both the westerly wind burst and strong convection reached the maximum strength near 4 February 1993. The strength is weaker for the second MJO than the first MJO, likely due to a cooler SST. The second peak of SST in the southern warm pool is 0.4 °C cooler than the first peak, due to a

shorter duration of heating. The convection associated with the second super cloud cluster is thus weaker than the first one, as less water vapor associated with a cooler SST is available to form clouds. The weaker second super cloud cluster in turn induces a weaker second westerly wind burst. Also different from the first MJO, there is no time-lag between the strong westerly winds and large cloud amount during the second MJO. This results from the absence of strong westerly winds associated with convection in the central Pacific, due to a cooler SST and weaker convection as compared to the first MJO.

Figure 9c shows that the temporal variability of the mixed-layer depth derived from (2) and (3) follows closely that of the wind stress. The mixed layer in the southern warm pool is generally very shallow, ~20 m, and deepens during the westerly wind bursts reaching ~70 m, with a mean of 28 m for the IOP. Figure 9d shows that the estimated solar radiation penetrating through the bottom of the mixed layer, f(h) F_{SW}, is significant in the southern warm pool as the mixed layer is shallow, except during the westerly wind burst of the first MJO. As a result, the rate of change in the SST does not follow the net surface heat flux, F_{net}, except during the westerly wind burst of the first MJO (Figs. 9a and 9d). Thus the penetration of solar radiation through the mixed layer in the southern warm pool is important to the mixed-layer heat budget and SST variation, in agreement with the conclusions of Anderson et al. (1996) and Sui et al. (1997).

The SST, surface fluxes and mixed-layer heat budgets shown in Fig. 10 for the northern warm pool present a very different picture from that of the southern warm pool. The northeasterly trade wind intensified in the middle period of the IOP, 11 December 1992-21 January 1993 (Fig. 10c). This seasonal intensification of the trade wind induces a large increase in F_{LH}, but only a slight decrease in F_{SW} (Fig. 10b). As a result, the net surface heating F_{net} decreases significantly with a minimum of -130 W m^{-2} (Fig. 10d). Before and after this period, F_{net} is close to zero. Consistent with F_{net}, the SST decreases during this period except 11-21 January 1993 and remains nearly unchanged before and after this period (Fig. 10a). This is a result of deep mixed-layer in the northern warm

pool and, hence, the small solar radiation penetrating through the bottom of the layer (Figs. 10c and 10d).

6. Conclusions

Using satellite radiance measurements, the heat and momentum fluxes at the surface of the Pacific warm pool have been derived for the COARE Intensive Observing Period, November 1992-February 1993. Daily values of the satellite-retrieved fluxes in the vicinity of the IMET buoy during the IOP are in good agreement with that of the buoy measurements. Averaged over the three time legs of the RV Moana Wave observation, there is also good agreement between the satellite-retrieved fluxes and the fluxes measured at the IMET buoy, RV Moana Wave, and RV Wecoma. These results show that the retrieved surface fluxes can be used to study the surface heat budget over the warm pool.

The characteristics of surface heat and momentum fluxes during the IOP are very different between the southern warm pool and the northern warm pool. In the southern warm pool, winds are generally weak except during short episodes of westerly wind bursts. As a result, the solar heating at the surface is much larger than the evaporative cooling. Averaged over the southern warm pool and the IOP, it is 196 W m^{-2} for the solar heating and only 108 W m^{-2} for the evaporative cooling, and the impact of the two MJOs on the surface solar flux is significantly larger than the impact on the latent heat flux. The monthly variation of the net surface heat flux is dominated by the solar radiation. Associated with the weak surface winds, the ocean mixed layer in the southern warm pool is shallow with a mean depth of ~28 m. Because of the shallow mixed layer, a significant amount of solar radiation incident at the surface penetrates through the bottom of the mixed layer (~45 W m^{-2}), and the rate of change in the surface temperature does not follow the net surface heat flux.

In the northern warm pool, the northeasterly trade wind averaged over the IOP is strong with a maximum > 8 m s^{-1}. The domain-averaged latent heat flux during the IOP is 148 W m^{-2}, which is much larger than the latent heat flux in the southern warm pool.

The monthly variation of the net surface heat flux is dominated by the latent heat flux which is, in turn, dominated by the seasonal change in the strength of the northeasterly trade wind. Because of the strong surface wind, the mean mixed layer is deep, ~56 m, and the solar radiation penetrating through the bottom of the mixed layer is small. The rate of change in SST during the IOP follows closely the net surface heat flux. Also different from the southern warm pool, the MJOs does not have a clear impact on the surface heat budgets of the northern warm pool.

Averaged over the IOP, ocean gains heat in the summer (southern) hemisphere while loses heat in the winter (northern) hemisphere, with the net heat flux ranging from -80 W m^{-2} in the northeastern section of the warm pool to 40 W m^{-2} north of New Guinea. Averaged over the warm pool and IOP, the net heating is only 0.7 W m^{-2}. This result is consistent with the studies of Godfrey and Lindstrom (1989) and Godfrey et al. (1991) that the mean surface net heat flux into the warm pool is small.

Acknowledgments

This study was supported by the TRMM Program and Radiation Research Program, NASA/Office of Earth Science. Daily SSM/I air-sea turbulent fluxes were processed by Chung-Lin Shie and Joe Ardizzone.

7 REFERENCES

Anderson, S. P., R. A. Weller, and R. B. Lukas, 1966: Surface buoyancy forcing and the mixed layer of the western Pacific warm pool: observations and 1D model results. *J. Climate*, 9, 3056-3085.

Atlas, R., R. N. Hoffman, S. C. Bloom, J. C. Jusem, and J. Ardizzone, 1996: A Multiyear Global Surface Wind Velocity Dataset Using SSM/I Wind Observations. *Bull. Amer. Meteor. Soc.*, 77, 869-882.

Chou, M.-D., W. Zhao and S.-H. Chou, 1998: Radiation budgets and cloud radiative forcing in the Pacific warm pool during TOGA COARE. *J. Geophys. Res.*, 103, 16967-16977.

Chou, S.-H., R. M. Atlas, C.-L. Shie and J. Ardizzone, 1995: Estimates of surface humidity and latent heat fluxes over oceans from SSM/I data. *Mon. Wea. Rev.*, 123, 2405-2425.

Chou, S.-H., C.-L. Shie, R. M. Atlas, and J. Ardizzone, 1997: Air-sea fluxes retrieved from Special Sensor Microwave Imager data. *J. Geophys. Res.*, 102, 12705-12726.

Enfield, D. B. 1986: Zonal and seasonal variations of the near-surface heat balance of the equatorial Pacific Ocean. *J. Phys. Oceanogr.*, 16, 1038-1054.

Fairall, C., E. F. Bradley, D. P. Rogers, J. B. Edson, and G. S. Young, 1996: Bulk parameterization of air-sea fluxes for Tropical Ocean Global Atmosphere Coupled Ocean-Atmosphere Response Experiment. *J. Geophys. Res.*, 101 (C2), 3747-3764.

Godfrey, J. S., and E. J. Lindstrom, 1989: On the heat budget of the equatorial west Pacific surface mixed layer. *J. Geophy. Res.*, 94, 8007-8017.

Godfrey, J. S., M. Nunez, E. F. Bradley, P. A. Coppin, and E. J. Lindstrom, 1991: On the net surface heat flux into the western equatorial Pacific. *J. Geophy. Res.* 96, 3343-3357.

Gutzler, D., G. N. Kiladis, G. A. Meehl, K. M. Weickman, and M. Wheeler, 1994: The global climate of December 1992-February 1993. Part II: Large-scale variability across the tropical western Pacific during TOGA COARE. *J. Climate*, 7, 1606-1622.

Jerlov, N. G., 1968: *Optical Oceanography*. Elsevier, 194 pp.

Lau, K.-M., C.-H. Sui, 1997: Mechanism of short-term sea surface temperature regulation: observations during TOGA COARE. *J. Climate*, 10, 465-472.

Lin, X. and R. H. Johnson, 1996: Kinematic and thermodynamic characteristics of the flow over the western Pacific warm pool during TOGA COARE. *J. Atmos Sci.*, 53, 695-715.

Lukas, R., and E. Lindstrom, 1991: The mixed layer of the western equatorial Pacific Ocean. *J. Geophy. Res.*, 96 (suppl.), 3343-3357.

Madden, R. A. and P. R. Julian, 1994: Observations of the 40-50 day tropical oscillation - a review. *Mon. Wea. Rev.*, 122, 814-837.

Niiler, P., and E. B. Kraus, 1977: One-dimensional models of the upper ocean. Modelling and Prediction of the Upper Layers of the Ocean, E. B. Kraus, Ed., Pergamon Press, 142-172.

Niiler, P., and J. Stevenson, 1982: The heat budget of tropical warm pools. *J. Mar. Res.*, 40 (suppl.), 465-480.

Paulson, C. A., and J. J. Simpson, 1977: Irradiance measurements in the upper ocean. J. Phys. Oceanogr., 7, 1722-1735.

Reynolds, R. W. and T. M. Smith, 1994: Improved global sea surface temperature analyses. *J. Climate, 7,* 929-948.

Schulz, J., P. Schluessel and H. Grassl, 1993: Water vapor in the atmospheric boundary layer over oceans from SSM/I measurements. *Int. J. Rem. Sens., 14,* 2773-2789.

Sui, C.-H., X. Li, K.-M. Lau, and D. Adamac, 1997: Mutiscale air-sea interactions during TOGA COARE. *Mon. Wea. Rev.*, 125, 448-462.

Webster, P. J. and R. Lukas, 1992: TOGA COARE: The TOGA coupled ocean-atmosphere response experiment. *Bull. Amer. Meteor. Soc., 73,* 1377-1416.

Weller, R. A. and S. P. Anderson, 1996: Surface meteorology and air-sea fluxes in the western equatorial Pacific warm pool during the TOGA Coupled Ocean-Atmosphere Response Experiment. *J. Climate*, 9, 1959-1990.

Wentz, F. J., 1994: *User's Manual SSM/I -2 Geophysical Tapes.* Tech. Rep. 070194, 20 pp. [Available from Remote Sensing Systems, Santa Rosa, CA.]

TABLE CAPTIONS

Table 1. Comparison of retrieved air-sea fluxes with those measured at the IMET buoy (1.75°S, 156°E) during COARE IOP. The SD error denotes the standard deviation of retrieved fluxes from that measured at IMET. Units are W m^{-2} for heat fluxes and 10^{-4} N m^{-2} for wind stress.

Table 2. Time-mean surface fluxes derived from satellite measurements (Sat) and from surface observations at RV Moana Wave (MW), RV Wecoma (Wec), and IMET buoy for three legs during COARE IOP. Units are W m^{-2} for heat fluxes, and 10^{-4} N m^{-2} for wind stress.

Table 3. Monthly and IOP mean surface heat budgets and relevant parameters averaged over the Pacific warm pool (135°E-175°E, 10°S-10°N).

Table 1. Comparison of retrieved air-sea fluxes with those measured at the IMET buoy (1.75°S, 156°E) during COARE IOP. The SD error denotes the standard deviation of retrieved fluxes from that measured at IMET. Units are W m^{-2} for heat fluxes and 10^{-4} N m^{-2} for wind stress.

Flux	Mean	Bias	SD error			Correlation
			Daily	Monthly	IOP	
F_{SW}	196.6	1.8	32.5	5.9	3.0	0.86
F_{LW}	50.9	-7.1	5.2	0.9	0.5	0.75
F_{SH}	6.3	-2.6	6.1	1.1	0.6	0.40
F_{LH}	104.8	-2.4	29.1	5.3	2.7	0.71
F_{net}	34.6	13.8	48.2	8.8	4.4	0.82
τ	371	-18	210	38	19	0.78

Table 2. Time-mean surface fluxes derived from satellite measurements (Sat) and from surface observations at RV Moana Wave (MW), RV Wecoma (Wec), and IMET buoy for three legs during COARE IOP. Units are W m^{-2} for heat fluxes and 10^{-1} N m^{-2} for wind stress.

Flux	Leg 1 (11/4-12/3/92)				Leg 2 (12/20/92-1/11/93)				Leg 3 (1/27-2/3/93)			
	Sat	MW	IMET	Wec	Sat	MW	IMET	Wec	Sat	MW	IMET	Wec
F_{SW}	231.0	224.7	227.8	223.1	175.6	162.0	162.3	168.2	182.9	164.0	180.3	192.8
F_{LW}	56.5	62.9	64.4	62.2	48.9	52.0	52.7	55.5	51.7	53.6	55.0	59.5
F_{SH}	5.0	6.0	6.8	4.6	6.2	8.4	10.0	9.1	7.4	9.4	8.3	13.4
F_{LH}	79.4	89.7	84.6	86.1	128.1	118.8	110.1	120.3	130.1	137.6	139.3	149.6
F_{net}	90.1	66.2	71.9	70.3	-7.7	-17.2	-10.5	-16.7	-6.3	-36.6	-22.4	-30.2
τ	198	205	183	174	537	638	653	636	542	535	546	567

Table 3. Monthly and IOP mean surface heat budgets and relevant parameters averaged over the Pacific warm pool (135°E-175°E, 10°S-10°N).

Parameter	Units	Nov 92	Dec 92	Jan 93	Feb 93	IOP
F_{SW}	W m^{-2}	196.3	185.8	196.4	193.2	192.9
F_{LW}	W m^{-2}	53.4	53.7	54.4	52.2	53.4
F_{LH}	W m^{-2}	114.7	151.4	138.4	121.4	131.9
F_{SH}	W m^{-2}	7.3	7.6	6.7	6.0	6.9
F_{net}	W m^{-2}	20.9	-26.7	-2.9	13.7	0.7
τ	10^{-4} N m^{-2}	410	660	680	620	590
SST	°C	29.14	29.05	28.63	28.51	28.84
$\partial T_S/\partial t$	°C $month^{-1}$	0.30	-0.68	-0.03	-0.09	-0.14
$SST-T_{2m}$	K	1.1	1.0	0.9	0.8	0.9
Q_S-Q_{10m}	g kg^{-1}	5.4	5.9	5.4	4.7	5.4
U_{10m}	m s^{-1}	5.2	6.4	6.5	6.5	6.1
T_B	K	271.7	268.4	272.9	267.4	270.1
W	g cm^{-2}	5.1	5.0	5.0	5.1	5.0

FIGURE CAPTIONS

Figure 1. Daily values at the surface for (a) net shortwave radiation, F_{SW}, (b) net longwave radiation, F_{LW}, (c) sensible heat flux, F_{SH}, (d) latent heat flux, F_{LH}, (e) wind stress, τ, and (f) net heat flux, F_{net}. Solid lines are surface measurements at IMET, while dashed lines, pluses and diamonds are satellite retrievals.

Figure 2. Mean fields of (a) net shortwave flux, F_{SW}, (b) net longwave flux, F_{LW}, (c) latent heat flux, F_{LH}, and (d) sensible heat flux, F_{SH}, at the surface for COARE IOP.

Figure 3. Mean fields of (a) GMS IR brightness temperature, T_B, (b) 10-m surface wind speed, U_{10m}, (c) sea-air humidity difference, (Q_S-Q_{10m}), and (d) sea-air temperature difference, $(SST-T_{2m})$, for COARE IOP.

Figure 4. Monthly mean surface net shortwave flux, F_{SW}. Regions of heating <190 W m^{-2} are shaded.

Figure 5. Monthly mean latent heat flux, F_{LH}. Regions of cooling <110 W m^{-2} are shaded.

Figure 6. Monthly mean net surface heat flux, F_{net}. Regions of cooling are shaded.

Figure 7. Mean fields of (a) net surface heat flux, F_{net}, (b) rate of SST change, $\partial T_S/\partial t$, and (c) penetration of solar radiation through bottom of mixed layer, f (h) F_{SW}, for COARE IOP.

Figure 8. Mean fields of (a) mixed-layer depth, h, and (b) scalar averaged wind stress, τ, for COARE IOP. Arrows are mean wind stress directions.

Figure 9. Time series of 5-day running mean (a) SST, (b) net surface solar flux, F_{SW}, and latent heat flux, F_{LH}, (c) mixed-layer depth, h, and scalar averaged wind stress, τ, and (d) net surface heat flux, F_{net}, and solar radiation penetrating through bottom of mixed layer, f(h) F_{SW}, averaged over the region 0-10°S and 135°E-175°E.

Figure 10. Same as Figure 9, except for the region 0-10°N and 135°E-175°E.

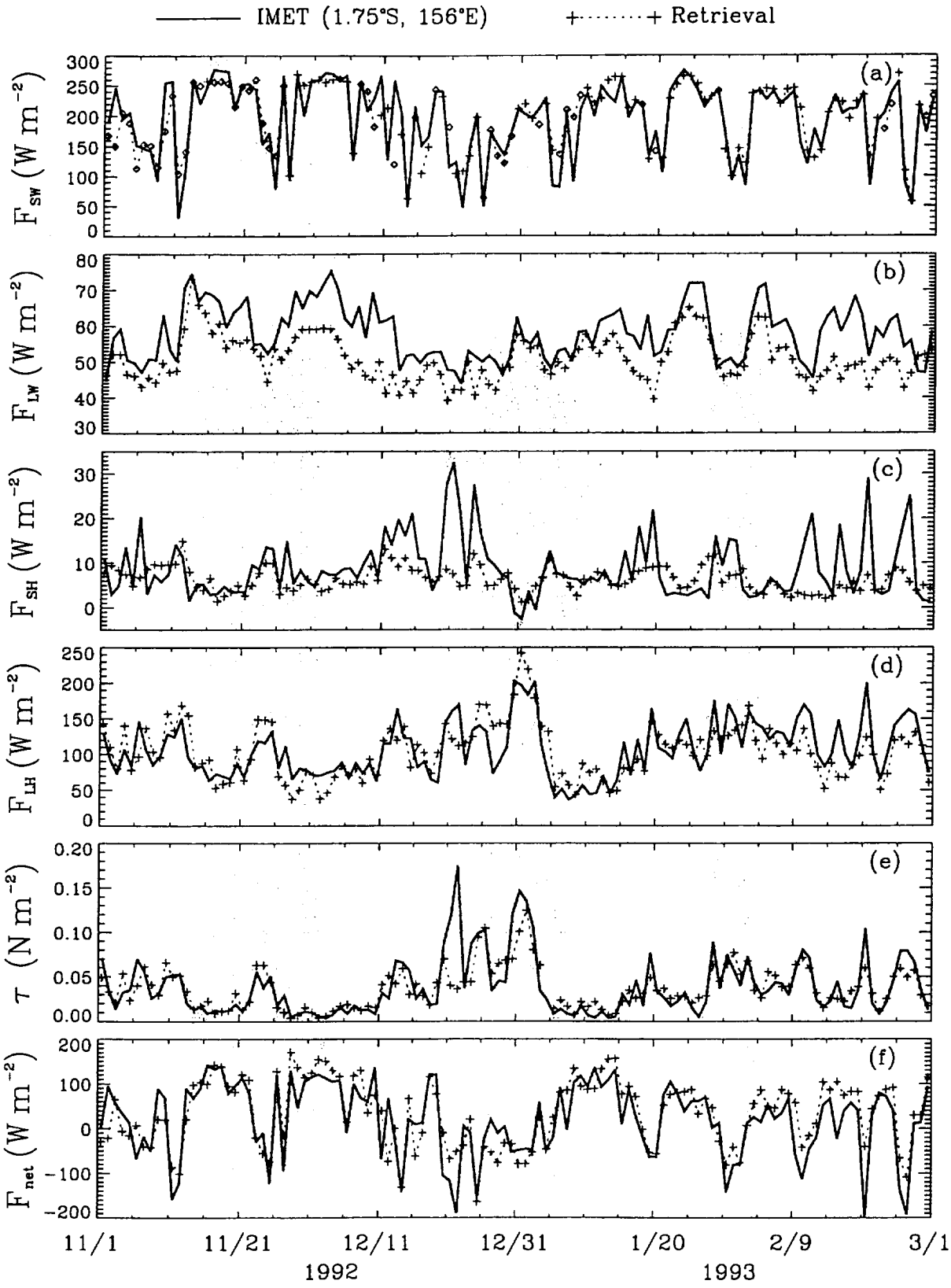
IMET (1.75°S, 156°E)
+·····+ Retrieval
(a)
F_{SW} (W m^{-2})
300
250
200
150
100
50
0
(b)
F_{LW} (W m^{-2})
80
70
60
50
40
30
(c)
F_{SH} (W m^{-2})
30
20
10
0
(d)
F_{LH} (W m^{-2})
250
200
150
100
50
0
(e)
τ (N m^{-2})
0.20
0.15
0.10
0.05
0.00
(f)
F_{net} (W m^{-2})
200
100
0
−100
−200
11/1
11/21
12/11
12/31
1/20
2/9
3/1
1992
1993

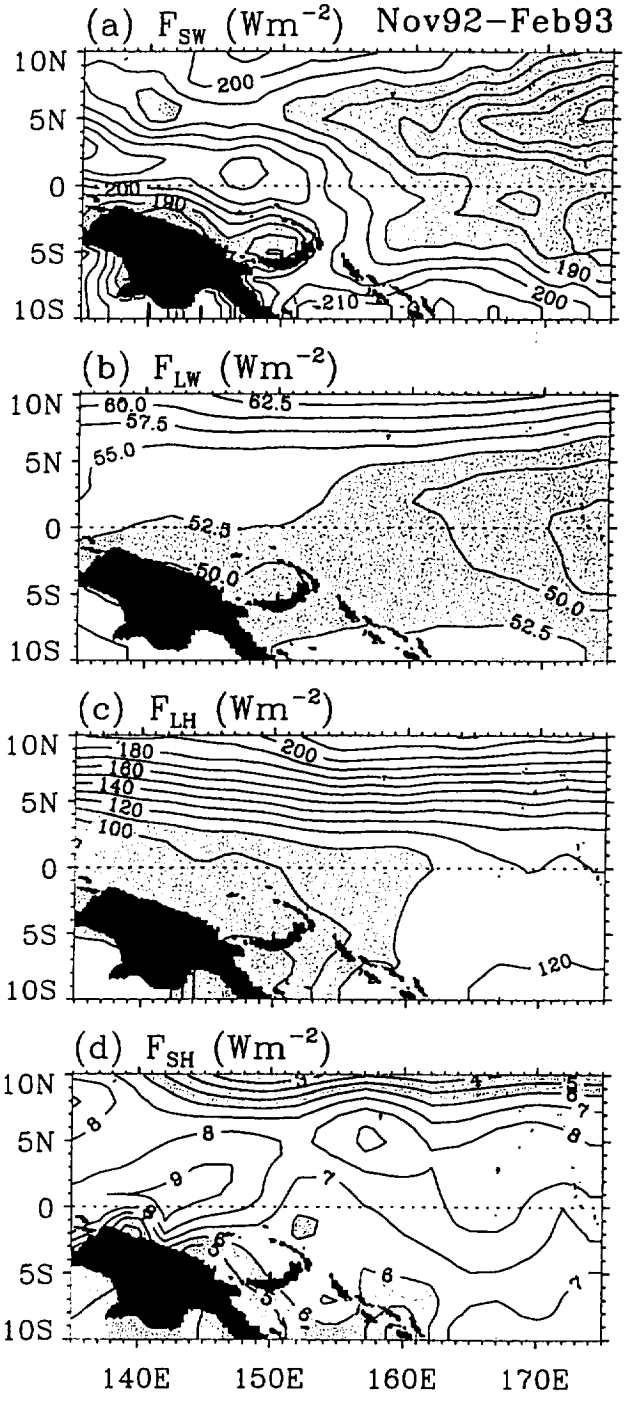
(a) F_{SW} (Wm^{-2}) Nov92–Feb93
10N
5N
0
5S
10S
200
190
210
(b) F_{LW} (Wm^{-2})
60.0
57.5
55.0
52.5
50.0
(c) F_{LH} (Wm^{-2})
180
160
140
120
100
200
(d) F_{SH} (Wm^{-2})
140E
150E
160E
170E

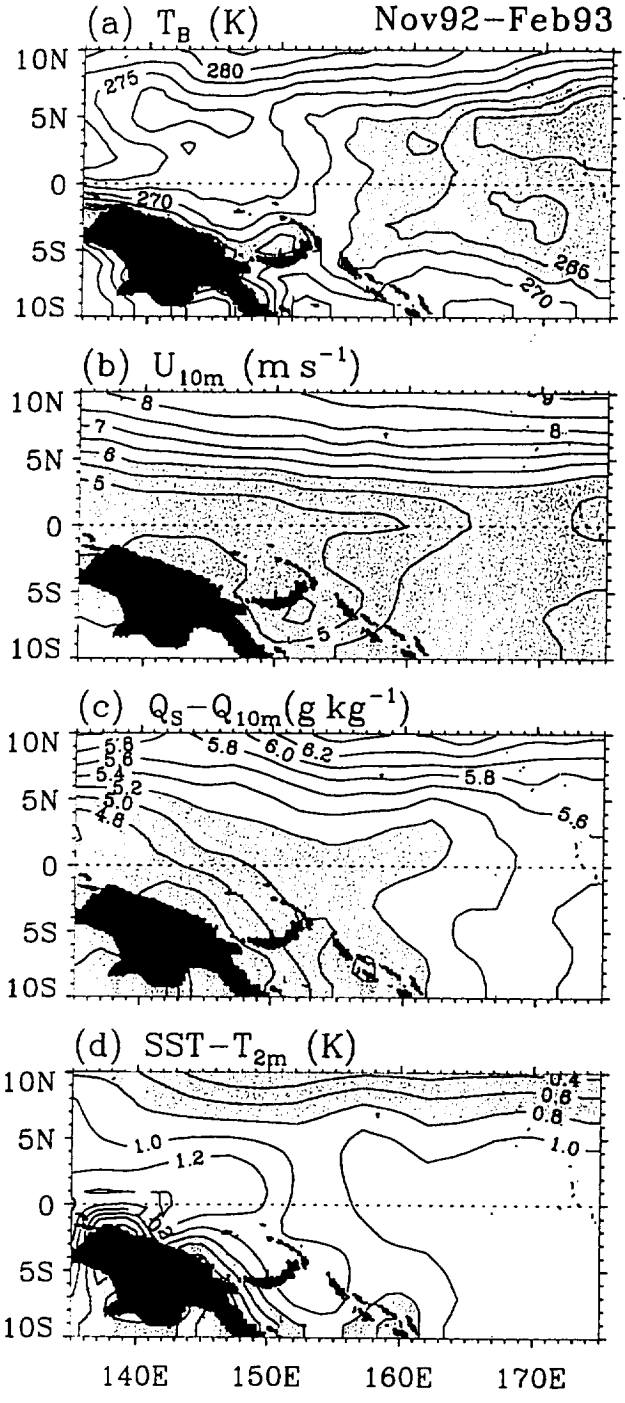
(a) T_B (K)
Nov92–Feb93
10N
5N
0
5S
10S
275
280
270
285
270
(b) U_{10m} ($m\ s^{-1}$)
8
7
6
5
8
5
(c) $Q_S - Q_{10m}$ ($g\ kg^{-1}$)
5.8
5.6
5.4
5.2
5.0
4.8
5.8
6.0
6.2
5.8
5.6
(d) SST – T_{2m} (K)
0.4
0.6
0.8
1.0
1.2
1.0
140E
150E
160E
170E

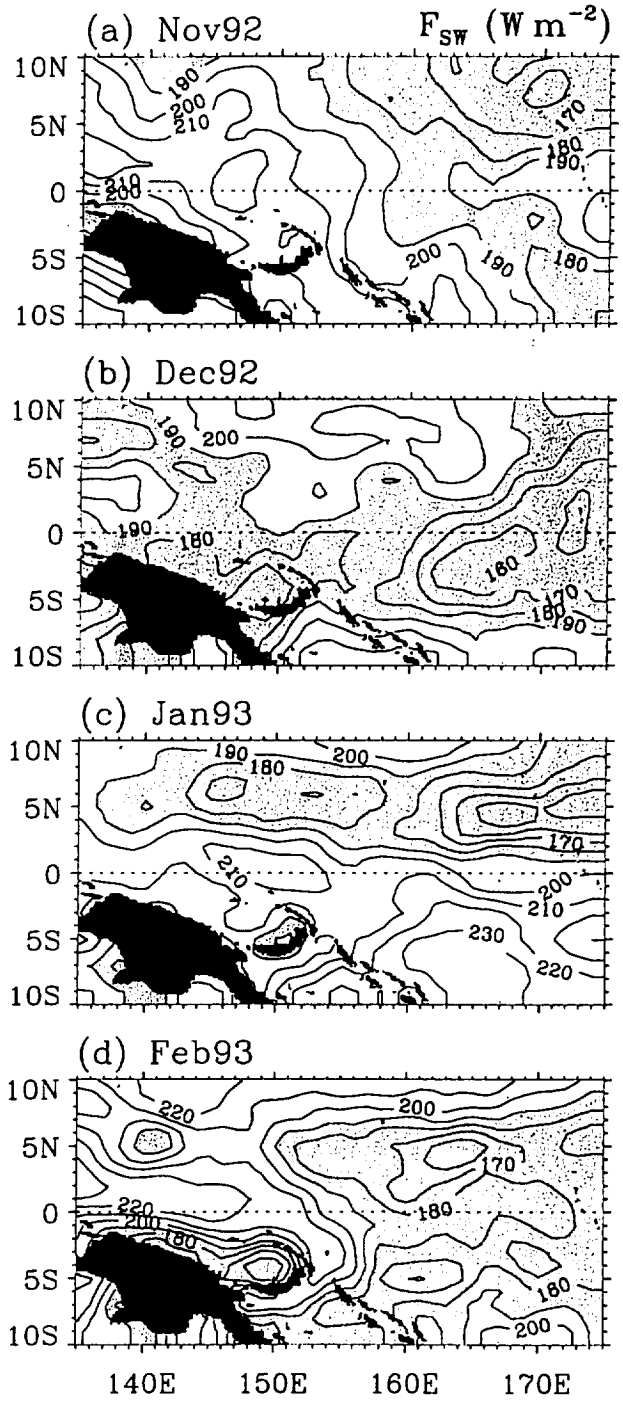
(a) Nov92
F_{SW} (W m^{-2})
(b) Dec92
(c) Jan93
(d) Feb93
10N
5N
0
5S
10S
140E
150E
160E
170E

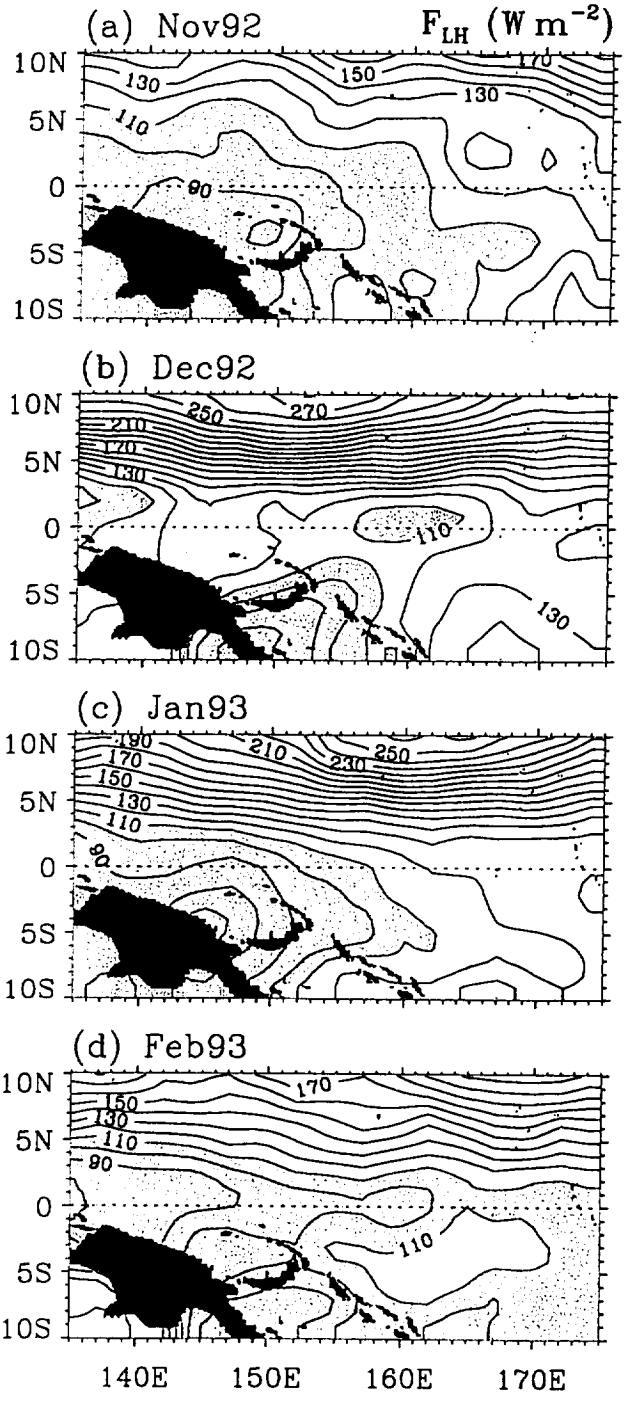
(a) Nov92
F_{LH} (W m^{-2})
10N
5N
0
5S
10S
130
150
110
90
170
(b) Dec92
250
270
210
170
130
110
(c) Jan93
190
210
230
250
170
150
130
110
90
(d) Feb93
170
150
130
110
90
140E
150E
160E
170E

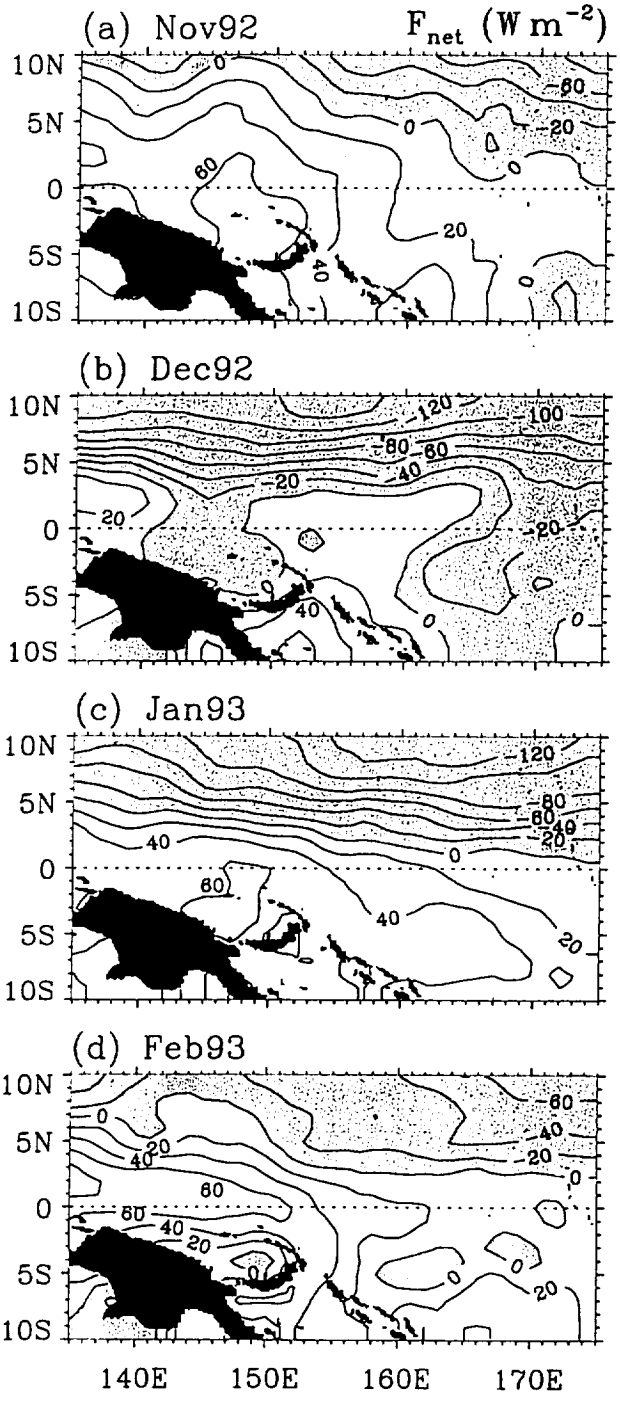
(a) Nov92
F_{net} (W m^{-2})
(b) Dec92
(c) Jan93
(d) Feb93
10N
5N
0
5S
10S
140E
150E
160E
170E

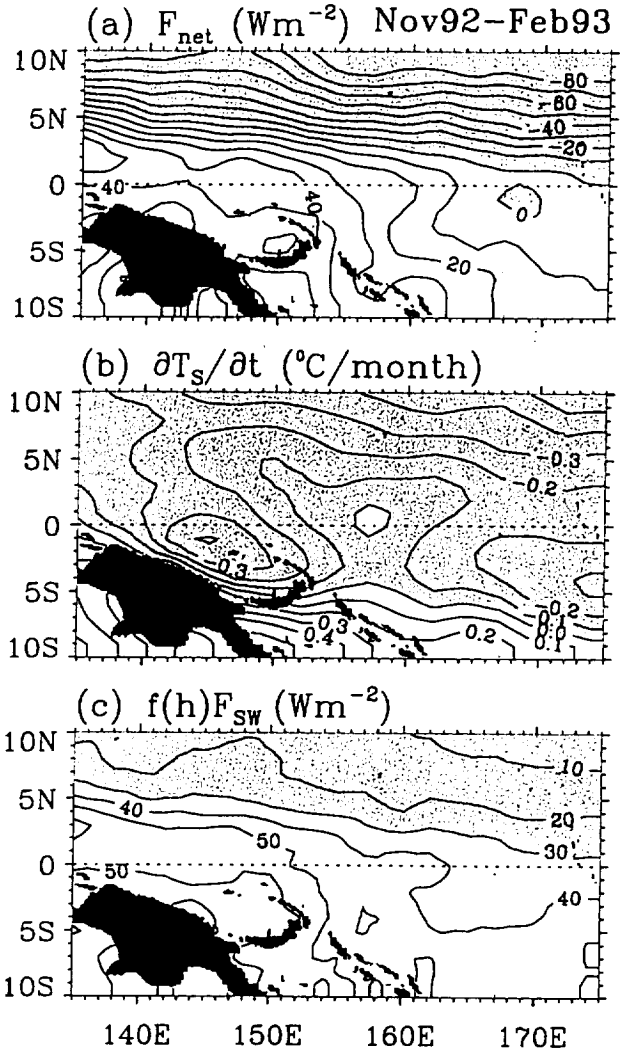
(a) F_{net} (Wm^{-2}) Nov92–Feb93
10N
5N
0
5S
10S
-80
-80
-40
-20
40
40
0
20
(b) $\partial T_s/\partial t$ (°C/month)
10N
5N
0
5S
10S
-0.3
-0.2
-0.3
-0.2
0.3
0.4
0.2
0.0
(c) $f(h)F_{SW}$ (Wm^{-2})
10N
5N
0
5S
10S
10
40
20
50
30
50
40
140E
150E
160E
170E

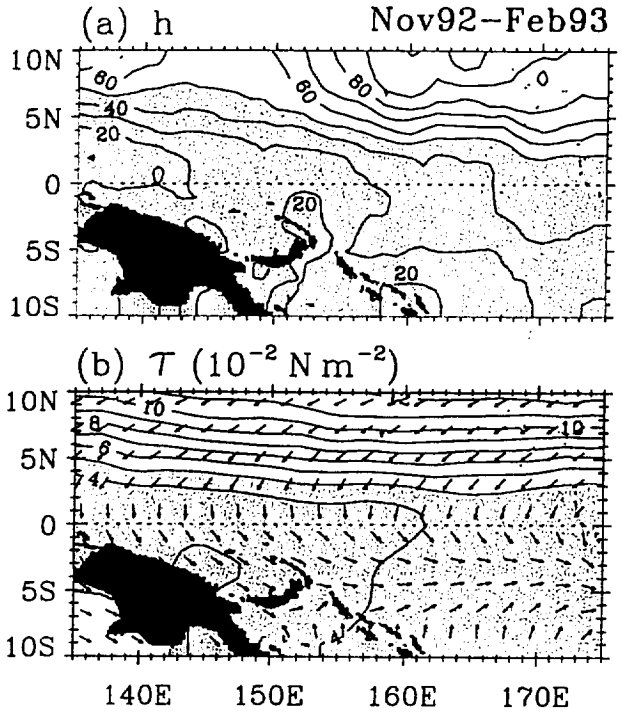
(a) h
Nov92–Feb93
10N
5N
0
5S
10S
60
40
20
0
80
20
(b) τ (10⁻² N m⁻²)
12
10
8
6
4
140E
150E
160E
170E

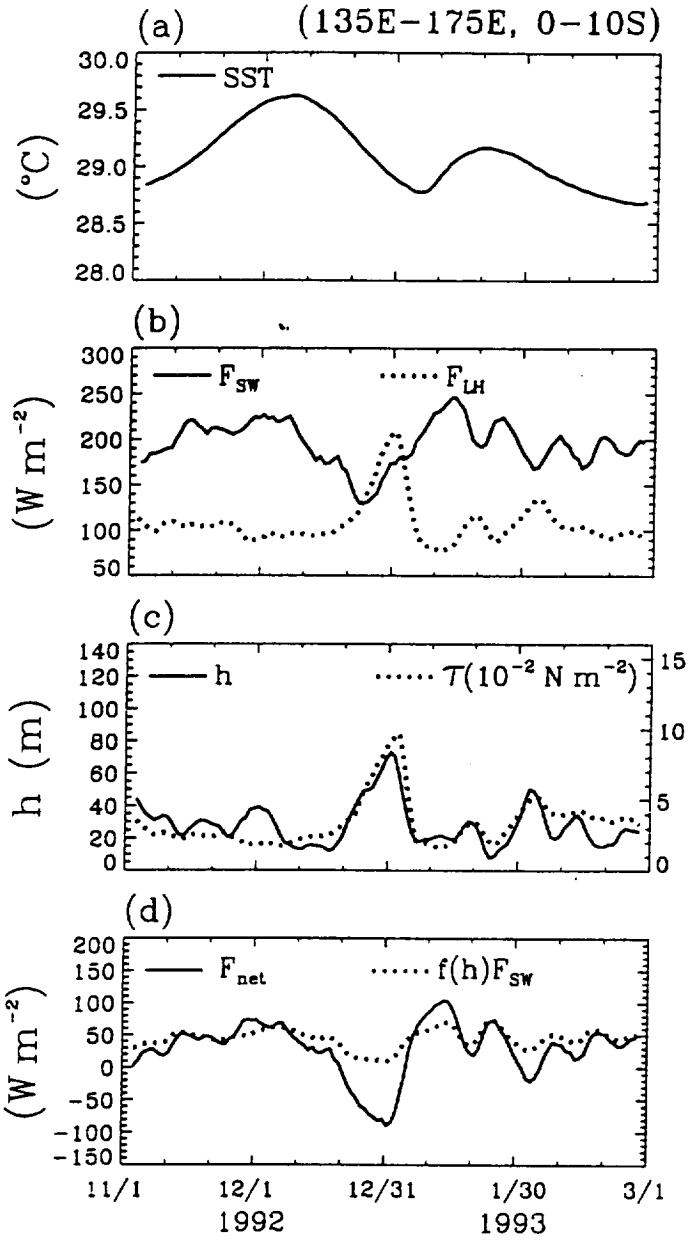
(a)
(135E−175E, 0−10S)
SST
(°C)
30.0
29.5
29.0
28.5
28.0
(b)
F_{SW}
F_{LH}
(W m^{-2})
300
250
200
150
100
50
(c)
h
$\tau(10^{-2}$ N m$^{-2})$
h (m)
140
120
100
80
60
40
20
0
15
10
5
0
(d)
F_{net}
$f(h)F_{SW}$
(W m^{-2})
200
150
100
50
0
−50
−100
−150
11/1
12/1
1992
12/31
1/30
1993
3/1

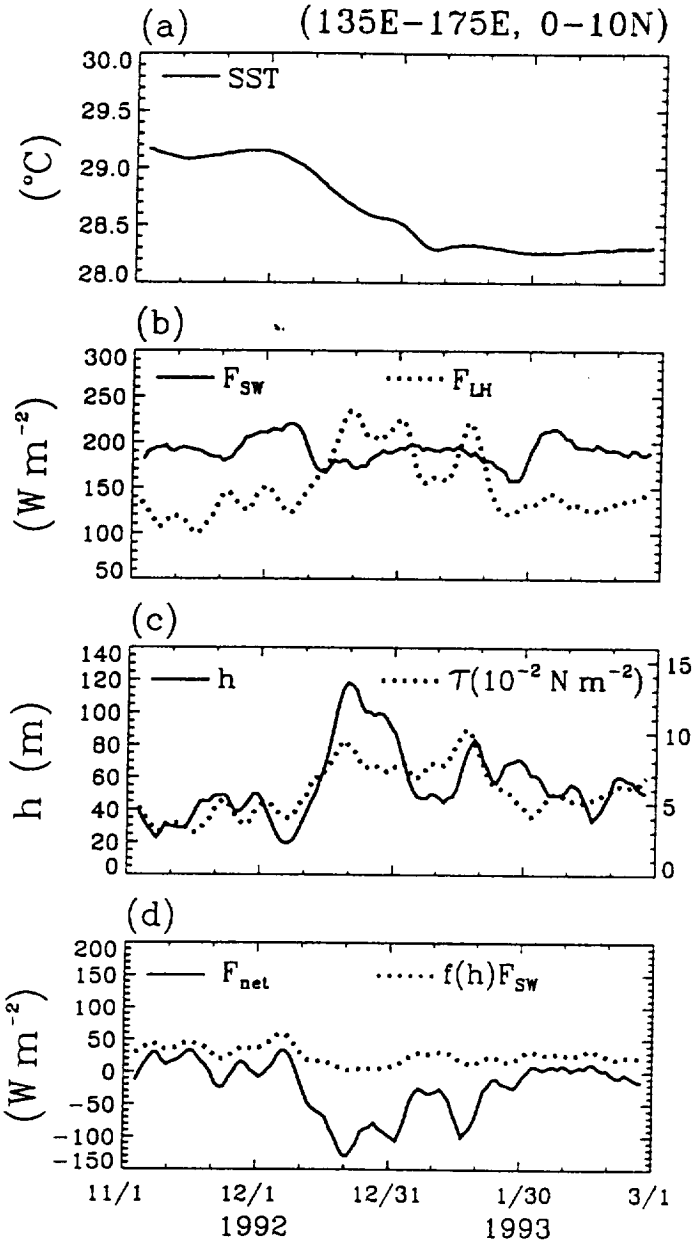
(a)
(135E−175E, 0−10N)
SST
(°C)
30.0
29.5
29.0
28.5
28.0
(b)
F_{SW}
F_{LH}
(W m^{-2})
300
250
200
150
100
50
(c)
h
$\tau(10^{-2}$ N m$^{-2})$
h (m)
140
120
100
80
60
40
20
0
15
10
5
0
(d)
F_{net}
f(h)F_{SW}
(W m^{-2})
200
150
100
50
0
−50
−100
−150
11/1
12/1
12/31
1/30
3/1
1992
1993